Soft and stretchable liquid metal transmission lines as distributed probes of multimodal deformations

Andreas Leber, Chaoqun Dong, Rajasundar Chandran, Tapajyoti Das Gupta, Nicola Bartolomei & Fabien Sorin*

Institute of Materials, École polytechnique fédérale de Lausanne, 1015 Lausanne, Switzerland.
*fabien.sorin@epfl.ch

Abstract:

Mechanical sensing represents a key functionality in soft electronics for applications in health monitoring, human–machine interaction, or soft robotics. Current approaches typically rely on intricate networks of sensors specific to one type of deformation and one point in space, severely limiting sensing capabilities. Here, we reconcile the concept of transmission line-based multimodal distributed sensing with the field of soft and stretchable electronics. We demonstrate the scalable fabrication of microstructured elastomeric fibers integrating tens of liquid metal conductors, with the length and the cross-sectional integrity necessary to successfully apply time-domain reflectometry. The materials' dynamic responsiveness drastically enhances collected signals compared to conventional transmission line probes, and enables the accurate detection of the mode, magnitude, and position of several simultaneous pressing and stretching events. Integrated within a large textile, an individual soft transmission line, interfaced through a single port, can decipher convoluted mechanical stimulation, bringing a new paradigm to advanced sensing in functional textiles and robotic skins.

Electronic skins and textiles are emerging as an enabling technology for developments in health monitoring[1–4], human–machine interaction[5,6], safety engineering[7,8], and soft robotics[9–11]. An essential functionality in these flexible and often stretchable systems is the detection of mechanical stimulation in the form of compression, elongation, bending, or torsion. However, quantifying and spatially resolving deformations of variable nature and number poses significant challenges to the design of proposed sensors. Strategies usually involve grids of point sensors on a flexible substrate, which, however, are limited in the kind of deformation they can sense, and must all be selectively addressed[12,13]. Alternatively, the necessary failure-susceptible contacts can be drastically reduced in number as well as positioned outside the sensing area by employing networks of functional fabrics[14,15], yarns[16], or fibers[17–19], which act as distributed sensors. The scalability of fabrication processes such as extrusion[20,21] or thermal drawing[22] make fiber-based systems particularly attractive in applications where large and flexible surfaces are sought to be functionalized. However, while fiber technology is often more receptive towards multimodal stimulation, only a single physical dimension, such as optical intensity[17,20] or electrical resistance[19], is typically monitored in a fiber-based sensor, hindering the decoupling of different types of deformation and the spatially resolved assessment of multiple stimuli.

Electrical time-domain reflectometry, a time-of-flight technique in which high-frequency pulses are sent down impedance-controlled transmission lines and are reflected at discontinuities, reveals both the nature and position of applied stimuli[23], making it a promising approach for the interrogation of distributed sensors. So far, the technique has been limited to static probes based on traditional hard conductors, employed primarily for the localization of structural faults[24–26] and the spatially resolved monitoring of dielectric characteristics of surrounding media[27–29]. Transferring time-domain reflectometry into the realm of soft materials is challenging, because the strict design principles of transmission lines constrain the engineering of materials and structure.

In this Article, we redefine the concept of transmission lines adapted to the field of flexible and stretchable electronics, by demonstrating several designs that integrate, in a scalable and precise way, liquid metal conductors in an elastomeric dielectric. We show that thermal drawing enables the

fabrication of transmission lines in large lengths and with uniform, targeted, and complex cross-sectional architectures. Beyond the control of radio frequency characteristics in soft transmission lines, including impedance, shielding, and losses, we investigate experimentally and theoretically reflected waves in the time-domain triggered by multimodal deformations of the dynamically responsive conductors themselves rather than only the dielectric between them. This unprecedented mechanism enables multiplexed pressure measurements at a sensitivity that is improved by a factor of 200 when compared to lines based on conventional rigid metals, as well as spatially resolved stretch sensing. On an exemplary 1 m-long line acting as a distributed probe, we demonstrate the quantitative assessment of multiple pressure points with a force resolution of 0.2 N and a spatial resolution of <6 cm as well as an elongation with a strain resolution of 0.25 %. By integrating a soft transmission line in a large stretchable fabric (50 cm x 50 cm), interfaced through a single contact point to cost-effective and easily available electrical instrumentation, we create an electronic textile with higher functionality than existing systems requiring hundreds of point sensors and electrical connections. This novel concept in fiber and textile-based sensing, easily implementable in various substrate materials and form factors, enables developments in soft electronics and robotics, electronic skins, and smart textiles.

Soft and stretchable liquid metal transmission lines design and fabrication

The stretchable transmission lines are composed of liquid metal alloy microchannels (65% Ga, 22% In, 10% Sn by weight) arranged within a thermoplastic elastomer dielectric (poly[styrene-b-(ethylene-co-butylene)-b-styrene], SEBS). Our fabrication approach relies on the preform-to-fiber thermal drawing technique, where the polymer is initially shaped by molding into a macroscopic preform and subsequently locally heated above its glass transition temperature and continuously drawn into a long and thin fiber (Fig. 1a). The liquid metal is injected into the polymer structure at the level of the preform for smaller diameter channels, where it takes a passive role during processing, or directly into the fibers for sufficiently large channels. SEBS is selected as the support material because of its rheological profile, distinguished by a high-viscosity flow at the processing temperature (Supplementary Fig. 1),

which enables the preservation of the cross-sectional geometry from the preform to the fiber[18,30]. The accurate and length-consistent placement of conductors in the dielectric is of outmost importance for efficient radio frequency transmission, as small deviations in size or spacing can sensitively influence operational parameters such as propagation constant and characteristic impedance.

To demonstrate the high level of control over material and process, we recreated transmission line designs common in the domain of hard materials through the arrangement of cylindrical microchannels in the elastic fibers, including two-wire, triangular, coaxial, and stripline (Fig. 1b). Notably, these complex structures can be realized over extended lengths of soft fiber (Fig. 1c), in which channels remain individually conductive but insulated from one another along the entire length, as illustrated by connecting the two poles of an LED through a long fiber (Fig. 1d). We demonstrate maintained conductivity under large, reversible deformations qualitatively by stretching a fiber, connected once more to an LED, to 100 % strain (Fig. 1e). We also assessed quantitatively the fiber's direct current resistance change during deformation by pressing and stretching (Fig 1f, g, respectively). These well-known behaviors in liquid-metal based systems[31–38] have proven beneficial for sensing applications, yet do not allow to discriminate between different deformations, or localize them in the system. Such sensitive and reversible changes of impedance can however be exploited, with the right coaxial design, for reflectometry-based sensing.

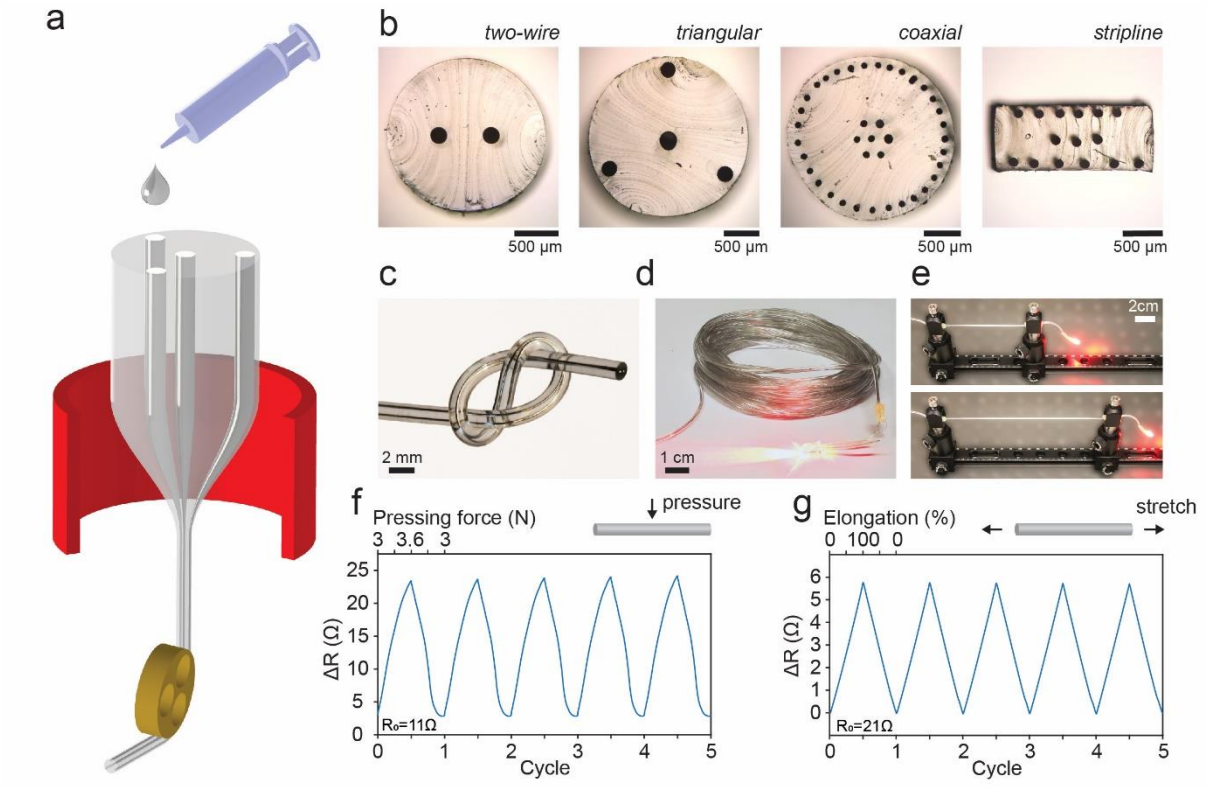

Fig. 1| Fabrication and structure of stretchable transmission lines. a, Schematic of the thermal drawing technique employed to process liquid metal-thermoplastic elastomer constructs into long fibers acting as transmission lines. **b,** Optical micrographs of line cross-sections as examples of commonly employed designs with targeted radio frequency characteristics, realized in soft constructs through the prescribed arrangement of Ga-In-Sn channels in SEBS. **c,** Photograph of a soft transmission line with two liquid metal conductors that run uniformly along its length. **d,** Photograph of a roll of transmission line connected to a power source on one end and an LED on the other end, demonstrating electrical conductivity through several insulated channels over extended lengths. **e,** Photographs of a line being stretched to 100% elongation with consistent conductivity, as shown by the unchanged brightness of the LED powered through the strained fiber. Change in resistance of a laterally compressed **(f)** and longitudinally stretched **(g)** line over several cycles.

Evaluation of soft transmission lines for time-domain reflectometry

We now turn to treating the microstructured fibers as transmission lines and interrogate them with electrical time-domain reflectometry. The experimental setup is schematized in Fig. 2a. A sharp step function, in our case with an amplitude of 0.5 V and a risetime of 100 ps, is produced by a pulse

generator and coupled into the line. The resulting voltage transient across the line end is monitored with an oscilloscope connected in parallel (Supplementary Fig. 2). Before introducing and characterizing line discontinuities, which cause partial reflections of the propagating signal, we assessed waveforms generated for soft transmission lines of different lengths (Fig. 1b). The produced signals are characteristic for open circuit-terminated lines; specifically, an abrupt initial rise as the step is first incident on the line, a near-constant voltage for the time of signal propagation through the line, and finally a full reflection at the end of the line. The characteristic impedance can be directly deduced from the waveforms (Supplementary Note 1) and is 89 ± 6 Ω. The travel time of the signal to the line end and back is proportional to the line length (Fig. 1b inset) and the propagation speed is found to be 1.95 x 10^8 $m.s^{-1}$. This value depends only on the relative permittivity of the dielectric medium[39], calculated here to be 2.38, which is consistent with the literature[40]. With the knowledge of the propagation speed, the time axis can be directly converted into distance units, enabling intuitive localization capability.

To evaluate the performance of fabricated transmission lines, we first test the shield quality for different structures by immersing line sections in ethanol and water with relative permittivities of 25 and 80[41], respectively. A comparison of the waveforms obtained for two disparate designs, two-wire and coaxial, are shown in Fig. 2c. For two-wire, the waveform exhibits an uneven profile, which depends on its interaction with the environment (Supplementary Fig. 3). As a medium of higher dielectric constant than air is introduced around a section of the line, a positive time shift of the open circuit termination reflection and a negative reflection at the interface of air to ethanol/water is observed (the effects are discussed in detail in Supplementary Note 2). While this behavior harbors a significant potential for spatially resolved materials diagnostics and monitoring of physical parameters[27–29], it is considered detrimental in this work dedicated to the unambiguous measurement of deformations. For the coaxial design, in contrast to two-wire, no discernable deviations in the smooth waveform occur when the line is introduced in a medium. The results for triangular and stripline design are detailed in Supplementary Fig. 4 and the shield performance for all considered designs is summarized in Fig. 2d, quantified by the time shift of the line end reflection due to the surrounding medium. While the coaxial line undergoes a

negligible time shift, it is closely followed by the triangular structure, which also stands out due to its simpler design, which eases line fabrication and connection.

To decouple effects originating from material and structure, as well as obtaining a baseline for the novel liquid metal lines, we compare their characteristics to more conventional solid metal lines with the same architecture and dimensions. The latter are fabricated in fiber-form through an adaption of the Taylor process[42], which involves Cu wires of diameter 250 µm being introduced into empty channels of an SEBS preform, and the thermal drawing of the assembly (Fig. 2e). The quantitative reasoning underlying the following discussion of losses is presented in Supplementary Note 3. In Fig. 2f, the attenuation coefficient is shown for three differently dimensioned triangular and a coaxial line based on liquid metal, as well as a triangular solid metal line. The attenuation coefficient of all considered lines follows roughly a square root relationship to the frequency, which is an indication of loss being dominated by the skin effect. This resistive loss depends on the conductor material, explaining the higher attenuation coefficient of lines based on Ga-In-Sn ($\sigma = 3.3 \times 10^6$ S m^{-1})[43] compared to Cu ($\sigma = 5.8 \times 10^7$ S m^{-1})[44]. Albeit limited by the material's resistivity, attenuation can also be tuned through structural changes. This includes an increase in conductor surface, which was implemented in the coaxial design through a division of the center and outer conductor into 7 and 32 microchannels, respectively. While the attenuation coefficient of the coaxial line is indeed lower than the triangular lines at lower frequencies, it increases at an elevated rate for frequencies above 1 MHz, presumably due to the proximity effect[45]. Alternatively, the resistive term of the attenuation coefficient can also be reduced by an increase in characteristic impedance, which is readily realized in triangular lines through a higher ratio of inter-conductor spacing to conductor diameter (Supplementary Fig. 5). The frequency-dependent attenuation in the transmission lines results in signal distortion in the time-domain[46], a detrimental effect observed in reflectometry measurements (Fig. 2b and Supplementary Fig. 6 and 7). As will be shown below, pulse broadening is the limiting factor for the spatial resolution of distributed probes consisting of liquid metal lines. In this regard, triangular designs with a higher characteristic impedance are considered promising candidates because they undergo lower losses.

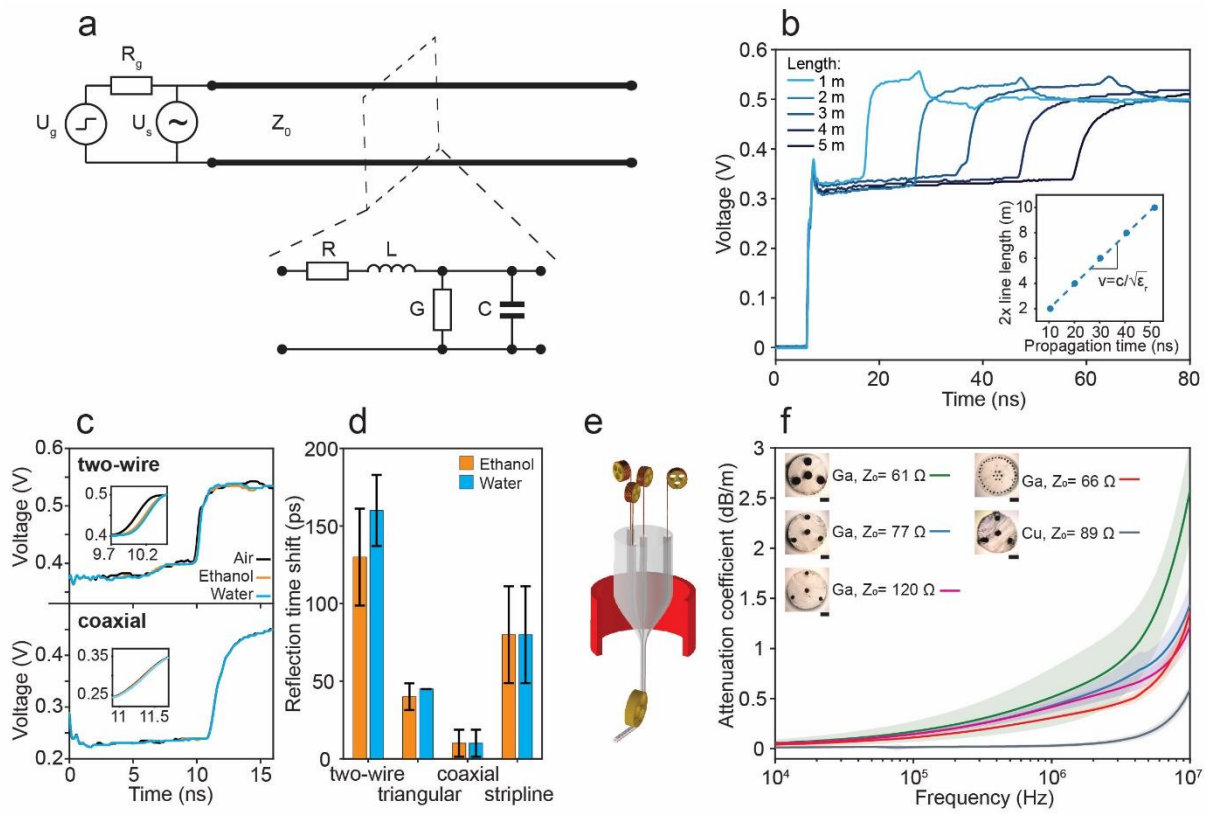

Fig. 2| Time-domain reflectometry setup and evaluation of transmission line performance. a, Circuit diagram of the reflectometry setup. A function generator with internal resistance R_g produces a step pulse with amplitude U_g that is applied to the interrogated transmission line with characteristic impedance Z_0 and open-circuit termination. The voltage across the transmission line as a function of time is monitored by an oscilloscope connected in parallel. In transmission line theory, an infinitesimal piece of line can be modeled as a lumped-element circuit with per-unit-length resistance R, inductance L, conductance G, and capacitance C. **b,** Time-domain reflectometry waveforms observed for liquid metal triangular transmission lines of increasing lengths. The inset shows twice the line length as a function of propagation time of the signal from line end to end and back. The slope of the resulting linear function corresponds to the propagation speed v, which can be approximated with only the speed of light in vacuum c and the relative permittivity of SEBS ε_r. **c,** Waveforms of two-wire and coaxial lines before and after a section is submersed in water and ethanol. The initial signal rise and connector ringing are cut for clarity. The insets show an enlarged plot of the reflection at the open-circuit termination, underlining the time delay induced by the medium for the two-wire line opposed to the unaffected coaxial line. **d,** Delay time induced by section-wise submersion of lines in water and ethanol for different transmission line types. The error bars represent the standard deviation. **e,** Schematic of thermal drawing with solid wires continuously fed into the created fiber during processing. **f,** Frequency-dependent attenuation coefficient of transmission lines

with different conductor materials (liquid metal Ga, solid copper Cu), structure type (triangular, coaxial), and characteristic impedance (Z_0). The solid lines represent the mean and the shaded areas the standard deviation.

Soft transmission lines as distributed probes of pressure and elongation

To deepen the understanding of the mechano-electrical coupling and highlight the value of employing liquid metals, we investigate the electrical response to pressing by comparing transmission lines composed of liquid metal microchannels to lines based on solid metal wires. The dielectric in both cases is the elastomer SEBS, and, thus, while not being stretchable, the solid metal-based lines are also compressible. In the test, a point force ramp is applied orthogonally halfway along the length of 1 m-long transmission lines (Fig. 3a). For both types, a larger force results in an increasing reflection at the time that corresponds to the pressing position along the lines. However, the shape of the reflected wave and the force magnitudes, under which the reflection occur, differ significantly. For the liquid metal lines, a positive step is produced in the waveform at forces as low as 2.5 N, which increases in amplitude at an approximate rate of 20 mV N^{-1}, whereas, for solid metal lines, a negative peak first appears at a larger force of 10 N and rises at a significantly smaller rate of approximately 0.1 mV N^{-1}. The dissimilar electrical responses are the result of the mechanisms under which the lines deform, schematized in Fig. 3b. Under increasing pressure, the channels collapse in a controlled fashion, thus increasing their resistance. In the solid wire-elastomer structure, however, only the spacings between the center and shield conductors vary, inducing a change in capacitance. With this knowledge, the magnitude of the discontinuities can be calculated based on the reflection in the waveforms (Fig. 3c and details in Supplementary Note 4). For the liquid metal transmission lines, the calculated resistance as a function of pressing force corresponds to previous measurements under direct current conditions (Fig. 1g) and exhibits similar advantageous force range, sensitivity, reversibility, and repeatability. For a measurement instrument with a voltage resolution of 4 mV, the sensitivity of 20 mV.N^{-1} implies a force resolution of the transmission line of 0.2 N on the loading path. In contrast, despite lower losses, the compressible Cu-wire transmission lines are considered poor pressure sensors because produced signals

are detectable only at large forces, and even under forces as large as 100 N the signals range on the order of fF (10^{-15} F), which represents a measurement near or beyond the limitations of most measurement instruments.

With the inherent spatial resolution of reflectometry, pressures can be both quantified and localized on the transmission lines. While the amplitude of a generated step in the waveform correlates to the pressing force magnitude, the time at which it occurs indicates the position of the pressure. From the waveforms generated for differently placed discontinuities, we extract the propagation times of the signal from the interrogated line end to the discontinuity and back (Fig. 3d). As shown, the propagation time is a linear function of the pressure position with the slope depending only on the propagation speed, which was previously determined for the dielectric SEBS. Thus, the permittivity of the employed dielectric represents the only parameter necessary for the accurate localization of pressures on the transmission lines and no sensor calibration is needed in applications, regardless of line length and diameter or contact resistance.

Furthermore, multiple pressure points on a transmission line, interrogated only from one end, can be simultaneously analyzed. To easily identify multiple discontinuities, we establish a resistance distribution from the collected waveform for the timespan that corresponds to the length of the line, revealing the pressure points on the transmission line (Fig. 3f). In the calculation of the distributed resistance, we considered that the second reflection is diminished by the first discontinuity, as the voltage wave is partly transmitted and reflected at every discontinuity. This recursive method is outlined in Supplementary Note 5. In the resistance profile, the two pressure points appear as distinct peaks. As the peaks are broadened by the finite bandwidth of the measurement instrument and the attenuation in the line, the magnitude of the point discontinuities on the line corresponds to a summation of the peak values. The maximum number of pressure points that can be simultaneously detected is dependent on the employed instrument's input voltage and the voltage resolution. In our case, reflections of a 500 mV step are detected at a resolution of 4 mV, resulting in a theoretical maximum of 125 pressure points. In this calculation, it is assumed that pressing forces are applied that induce voltage steps equal to the

resolution. Larger forces will reduce the number of points that can be detected, and, thus, the line must be arranged according to the expected pressure distribution to avoid cutting off parts of the line in real applications. The capabilities of the proposed sensor system can be extended by interrogating the line from both ends as well as employing multiple lines in application-targeted networks, representing two strategies commonly employed in the field of functional fibers and smart textiles[19,20,47].

We assess the spatial resolution experimentally by determining the minimum spacing between two pressure points of equal magnitude that can be resolved separately (Fig. 3g). When the line is loaded close to the interrogated end, shown here for 0.2 m, two pressure points distanced 8 cm from one another appear as sharp steps in the waveform and distinct peaks in the resistance profile. As the spacing is reduced, the peaks start to overlap up to the point where they merge into a single peak at a spacing of 2 cm, at which point they cannot be resolved separately anymore. We define the spatial resolution as the spacing, where the valley between the two peaks is equal to 70 % of the higher of the two peaks, corresponding here to 4 cm. However, the spatial resolution is not constant along the length of the line but depends on the distance of the pressure points to the interrogated end. Considering, for instance, the two pressure points being applied 4 m down the line, a broadening of the originally sharp peaks in the resistance profile is observed, an effect attributed to the signal attenuation in the lines, resulting in an increased spatial resolution of 18 cm. Through repetitions of this procedure at different distances from the interrogated end, the resolution is extracted as a function of position on the line (Fig. 3h), ranging from 4 cm at 0.2 m to 20 cm at 5 m (the complete data set is shown in Supplementary Fig. 8). As shown in the plot and discussed in Supplementary Note 6, the spatial resolution follows a quadratic dependency on the position. We conclude that the spatial resolution is dictated by the instrument for small distances but is quickly overtaken by line attenuation as the dominating resolution-limiting mechanism for pressure positions further down the line. In applications involving long lines and severe localization requirements, the lines can also be interrogated on both ends, resulting in an improved spatial resolution.

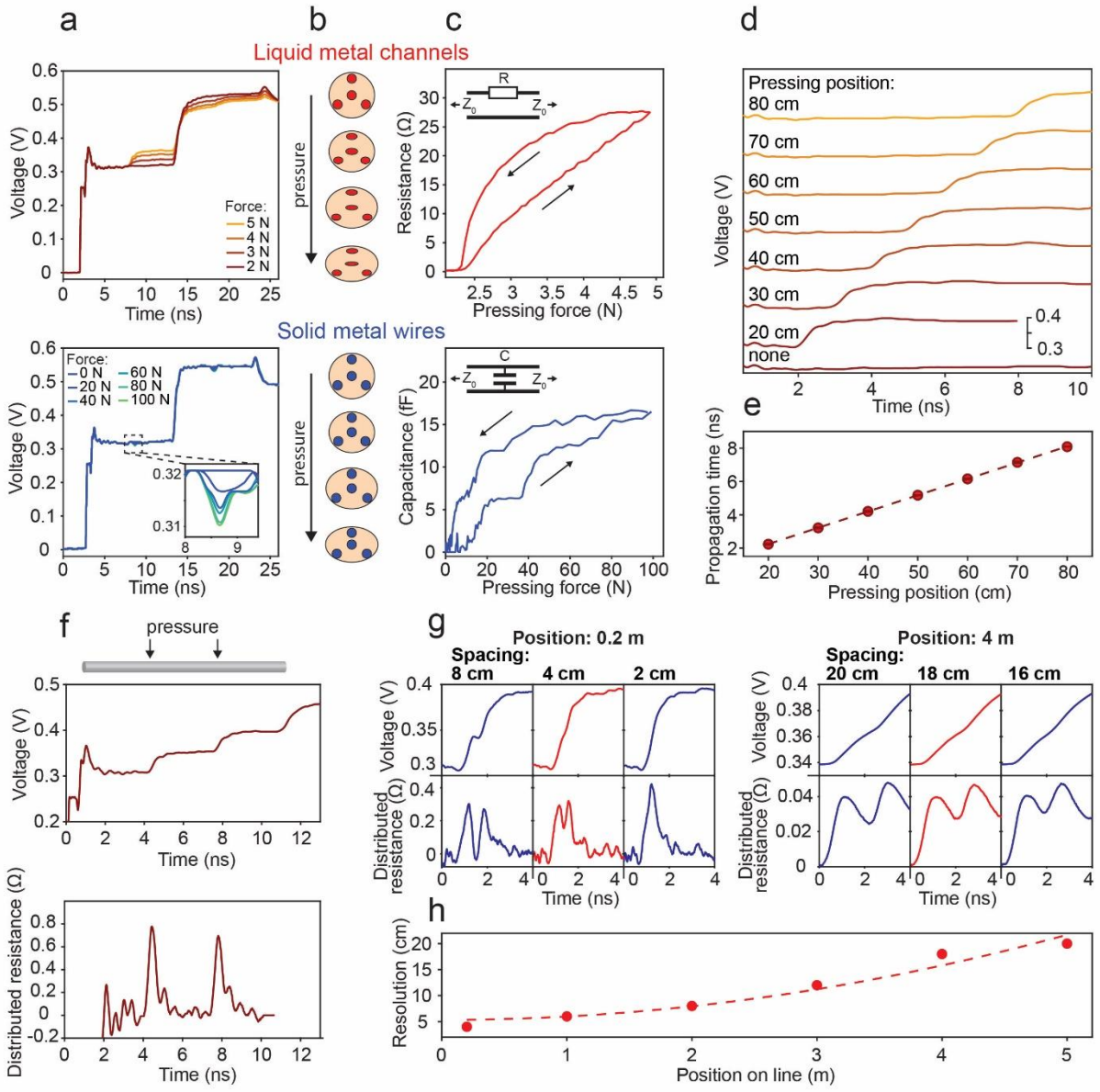

Fig. 3| Pressing on soft transmission lines. a, Waveforms of a liquid metal (top) and solid metal (bottom) triangular line of length 1 m loaded at 50 cm with an increasing pressing force. **b,** Schematic of the cross-sectional deformation mechanism of lines under increasing pressures. The liquid metal microchannels collapse in a controlled fashion (top), whereas the solid metal wires are unaffected and merely their spacing varied (bottom). **c,** Resistance R of a single series resistive discontinuity for liquid metal channels (top) and capacitance C of a single shunt capacitive discontinuity for solid metal wires (bottom) along the line of otherwise unchanged characteristic impedance Z_0 calculated based on the reflection in the waveforms as a function of pressing force. The loading and unloading path are indicated by arrows. **d,** Waveforms for pressing of equal force but varying position along liquid metal lines. The initial signal rise and connector ringing, as well as the final termination reflection are cut for clarity. **e,** Propagation time of the signal to the discontinuity and back as a function of pressing

position calculated from the waveforms. **f,** Two pressure points are applied at 33 cm and 66 cm from the interrogated end on a 1 m-long liquid metal line, inducing steps in the waveform (top). Based on the reflections in the line, a distributed resistance is established, in which the pressure points appear as distinct peaks (bottom). **g,** The spatial resolution of pressure sensing is investigated by applying two pressure points of equal magnitude at different positions from the interrogated end. The waveforms and distributed resistance profiles are shown for two positions and three different spacings between the two pressure points (top). The resolution is defined as the spacing where the valley in the distributed resistance profile between the two peaks is equal to 70 % of the higher of the two peaks, highlighted here in red. **h,** The extracted spatial resolution is shown as a function of position along the length of the transmission line probe.

Having established spatially resolved pressure sensing, we investigate the response of elongation from 0 to 100 % of the lines in time-domain reflectometry (Fig. 4a). By stretching the line, the open circuit termination reflection is shifted towards higher times due to the increased length. The relationship of propagation time to elongation is found to be linear (Fig. 4b), confirming an unchanged propagation speed in the stretched lines. Furthermore, the dependency is fully reversible with negligible hysteresis and exhibits a sensitivity of 0.1 ns $\%^{-1}$ for a 1 m-long line, implying a strain resolution of 0.25 % when using an instrument with a temporal accuracy of 25 ps. Note that, although plotted here as a function of the relative quantity strain, the propagation time yields directly the absolute length of a stretched line. Besides the time-shifted termination reflection, the voltage trace remains unchanged. This is, firstly, due to the low-loss nature of the line for which the characteristic impedance is dominated by capacitive and inductive rather than resistive contributions, and, secondly, because cross-sectional dimensions vary homogeneously when the line is stretched. Considering the simple geometry of a coaxial line[48], the characteristic impedance Z_0 as a function of strain e can be expressed as

$$Z_0(\mathrm{e}) \simeq \frac{1}{2\,\pi}\sqrt{\frac{\mu}{\varepsilon}}\,\ln\left(\frac{D(e)}{d(e)}\right) = \frac{1}{2\,\pi}\sqrt{\frac{\mu}{\varepsilon}}\ln\left(\frac{D_0\cdot(1-\nu e)}{d_0\cdot(1-\nu e)}\right) = \frac{1}{2\,\pi}\sqrt{\frac{\mu}{\varepsilon}}\ln\left(\frac{D_0}{d_0}\right)$$

where μ is the permeability, ε the permittivity, D and d the outer and inner conductor diameter respectively, and υ the Poisson ratio. Thus, the characteristic impedance remains constant for any elongation. The same reasoning can be made for the triangular transmission line design, which is more complex due to its discontinuous cross-sectional geometry (Supplementary Note 3).

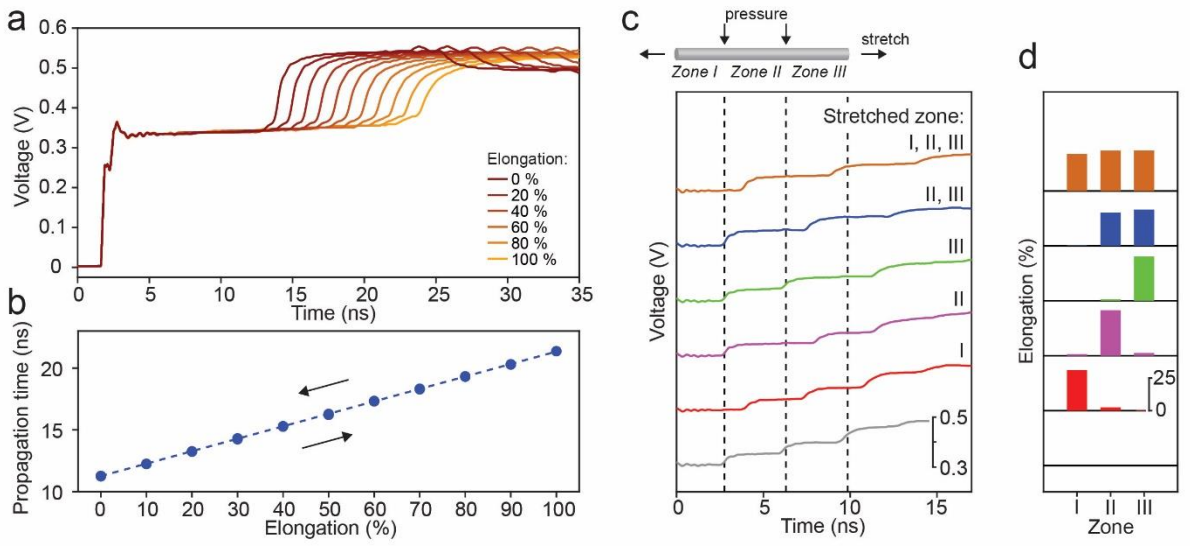

Fig. 4| Stretching of soft transmission lines. a, Waveforms of a liquid metal triangular line being stretched to increasing elongations, resulting in a time shift of the reflection at the open circuit termination. **b,** Propagation time of the signal in the line extracted from the waveforms as a function of applied elongation. The plot includes the loading and unloading path, which overlap near perfectly. **c,** A 1 m-long transmission line is locally compressed at 33cm and 66cm as a mean of discretizing the line into three zones for localized strain sensing. Selective stretching results in an increased propagation time in only the corresponding zones, as shown by a time shift of the steps in the waveform. **d,** Based on the change in propagation time, the elongation can be directly calculated for each zone, related for each loading case shown in c by the color.

While a constant characteristic impedance for arbitrarily stretched transmission lines may prove beneficial in communication, the lack of reflections hinders the localization of section-wise applied elongations in sensing applications. To obtain position information, we introduce discontinuities on the line to discretize it into sections. As previously shown, this is readily achieved for soft transmission lines by locally applying controlled pressures, generating steps in the waveform (Fig. 4c). As

elongations are applied selectively in one or several of the three created zones, the propagation time increases only in the corresponding sections, as indicated by a time shift of the voltage step (Fig. 4d). While this strategy demonstrates the ability of localizing and quantifying stretching in transmission lines, it proves impractical in applications where spatially resolved sensing of both stretching and pressing is targeted. In such use cases, discontinuities for discretization of a different nature, for instance capacitive which induce negative peaks in the waveform, can be introduced as not to interfere with the signals generated for pressing.

Multiplexed deformation sensing in electronic textile

The capabilities of the soft transmission line probes are demonstrated in practice by integrating a 10 m-long line on a stretchable piece of fabric of size 50 cm x 50 cm (Fig. 5a). A serpentine pattern with a spacing of 3 cm is selected, which enables the functionalization of the entire surface with an individual line, interfaced through a single point (Supplementary Fig. 9). The proposed spatially resolved sensing strategy based on a single sensor unit stands in contrasts to commonly employed grids of point sensors that must all be addressed selectively[12], but also networks of fiber-based sensors without spatial resolution[49,50]. Since specialized time-domain reflectometers are expensive, delicate, and large-footprint instruments, we employ a custom pulse generator with cost in parts of less than US$ 10 coupled with a standard oscilloscope. Although the produced signal exhibits some ringing and a higher rise time of 5 ns (Supplementary Fig. 10), limiting the positional accuracy to approximately 25 cm (Supplementary Fig. 11), it serves as a practical and cost-effective solution.

We submit the electronic textile to a series of tests, where controlled pressures and elongations are applied on the probe. First, an individual pressured point is applied by a finger (Fig. 5b), generating a step in the waveform and a peak in the distributed resistance profile, the height of which corresponds to the applied pressure. The peak value is shown for a complete cycle of pressing and releasing, demonstrating the continuity and reversibility of the measure. The waveform and resistance profile for

two snapshots, corresponding to a small and large pressure are shown in the main figure and additional data points are displayed in Supplementary Fig. 12. The time in the spectrum at which the resistance peak occurs reveals the position of the pressure point, determined here to be 4.92 m from the interrogated line end. As an intuitive visualization, the peak resistance values are laid out in a color-coded map, indicating the position and magnitude of a pressure event. Next, multiple pressure points are simultaneously applied on the functional textile to test the multiplexing capability of the probe (Fig. 5c). Indeed, the three applied pressure points appear as distinct peaks in the resistance profile and are accurately positioned on the spatial map. As a second mode of deformation, we stretch the fabric in the longitudinal line direction (Fig. 5d). Unlike pressing, this stimulation does not generate a local discontinuity in the waveform but increases the propagation time, quantified by a positive time-shift of the open circuit reflection. We display the line propagation time for a cycle of stretching and releasing, as well as two snapshots corresponding to a small and large strain. The procedure of extracting the propagation time is shown Supplementary Fig. 13. In a final test, we aim at the simultaneous detection of pressing and stretching based on the disparate responses of the two modes of deformation. Indeed, the signals can be successfully decoupled, and the two pressure points are accurately resolved as well as the elongation quantified (Fig. 5e). All loading scenarios displayed here are extracted from one experiment and the video and data stream are shown in Supplementary Video 1 and 2. The experiment underlines how the actual configuration of the large electronic textile, which may undergo convoluted changes in the form of pressures and stretches, can be reconstructed based on the time-domain reflectometry measure of a single probe interfaced through a single contact point.

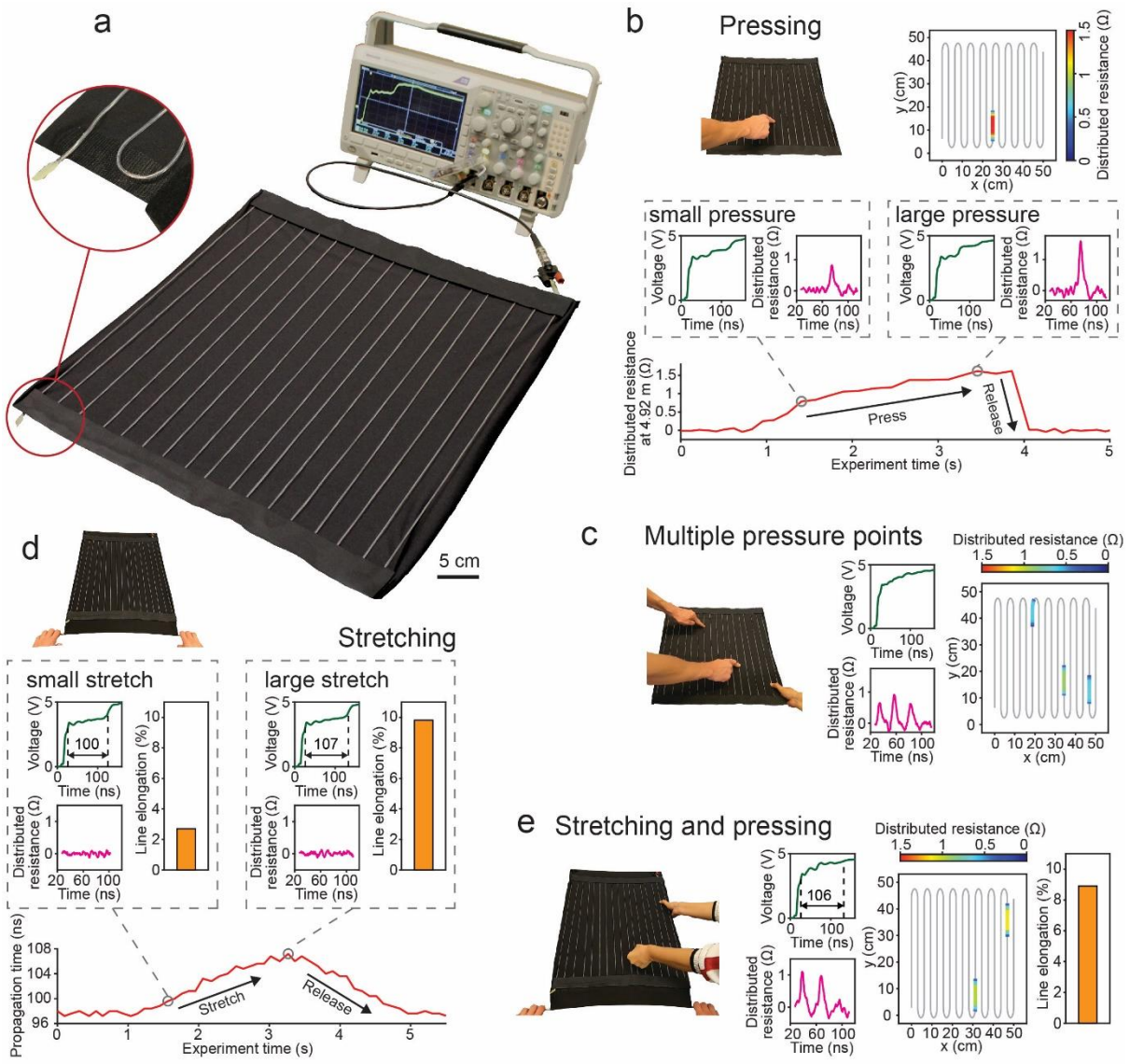

Fig. 5| Electronic textile for multiplexed deformation sensing. a, A 10 m-long triangular liquid metal transmission line probe is integrated in a serpentine pattern on a stretchable fabric and is interfaced through a single contact point. The inset shows the open circuit termination and one of the line loops that is fixed in the textile by Velcro strips. A custom pulse generator of small footprint and low cost coupled with a standard oscilloscope are used to interrogate the textile. **b,** An increasing pressure is applied by a finger on the textile. The waveform and distributed resistance are shown for a small and large pressure. The increase and subsequent decrease in calculated resistance at the position of the pressure point (4.92 m from the interrogated end) corresponds to the complete cycle of pressing and release, confirming a continuous pressure magnitude measurement. The peak resistance values are laid out in a two-dimensional color-coded spatial map according to the arrangement of the line on the textile, on which the location of the pressure event is accurately represented. **c,** Three pressure points are simultaneously applied on the textile, and their magnitude and position extracted from

the waveform, as shown by the three peaks in the distributed resistance profile and the highlighted sections in the map. **d,** The entire textile is stretched in the longitudinal line direction. Two snapshots in a stretching event are shown in the form of the waveform, on which the propagation time in the line is highlighted, the distributed resistance profile, which remains unchanged, and the line elongation that is directly calculated from a change in propagation time. The continuous measure of the propagation time is shown for a complete elongation cycle. **e,** The textile is simultaneously exposed to the two modes of deformation, stretching and pressing. The configuration of the textile is reconstructed based on waveform and visualized in the map, which shows the elongated shape of the textile as well as pressure points.

Conclusions

We have introduced a class of soft and stretchable transmission lines, which are composed of liquid metal microchannels arranged within a thermoplastic elastomer dielectric. Through the thermal drawing in a regime dominated by viscous forces, a diverse collection of cross-sectional architectures in the soft materials constructs is realized, which are uniform over extended lengths and act as transmission lines with controlled impedances, shielding, and losses. The experimental and theoretical exploration of the mechanisms of electromechanical coupling, where both soft and hard-soft hybrid structures are studied, reveal the unique capabilities of liquid metal lines that are converted into distributed probes of multimodal deformations through the interrogation by time-domain reflectometry, including high sensitivity, complete reversibility, and large deformation ranges. Our sensing approach is distinguished by the functionalization of large, flexible, and stretchable areas of various form factors with a single sensor unit interfaced through a single contact point, which includes a continuous measure of both magnitude and position of pressures and stretches. Based on the wealth of information that the proposed soft transmission lines produce, the convoluted mechanical stimulation in electronic textiles, wearable devices, and robotic skins can be reconstructed.

Methods

Fabrication and connections of soft transmission lines. *Liquid metal microchannel fibers.* Granules of SEBS (Kraton) were filled in a custom mold of the desired shape (cylindrical or rectangular), which included cylindrical cores of variable diameter fixed to the base plate, and the assembly was hot-pressed at 0.5 bar, 180 °C for 6 h. The polymer preform was thermally drawn into fibers using a custom draw tower at a maximum temperature of 160 °C and at variable take-up speeds, thus controlling the fiber diameter and length. The liquid metal Ga-In-Sn (Indium Corporation) was injected with a syringe into the structure before the drawing step for channels diameters smaller than 1 mm in the preform and directly into the fibers for larger preform channel diameters. Steel wires were inserted into the liquid metal channels at the fiber ends and the connection point sealed with an adhesive.

Solid metal wire fibers. The polymer preform was prepared as stated in the previous section. For the drawing process, Cu wires of diameter 250 µm (McMaster) were fed into the empty channels of the suspended preform, and the assembly thermally drawn at a temperature of 200 °C. As the polymer flowed into a fiber, the wires were caught by the narrowing channels and continuously unspooled as the polymer was drawn. Note that in our technique the wires do not melt or change shape otherwise. For connection, the wires at the fiber ends were stripped of the encapsulating polymer.

Direct current characterizations. *Pressing response test.* Fibers of length 1 m with liquid metal microchannels in the triangular configuration were short-circuited at the far end and connected to an electrometer (Keithley Sourcemeter 2400) at the near end with the center and outer conductors connected to the positive and negative pole, respectively. The fibers were locally and repeatedly compressed under controlled forces (3 N min^{-1}) in a dynamic mechanical analysis setup (DMA, TA Instrument DMA Q800), where a steel rod of diameter 6 mm positioned perpendicularly to the fibers served as an indenter. During the test, the direct current resistance, pressing force, and indenter displacement were continuously recorded.

Stretching response test. Fibers of length 15 cm with liquid metal microchannels in the two-wire configuration were short-circuited on one end and connected to the electrometer on the other end. Fiber sections of length 8 cm were repeatedly stretched in a custom linear motion drive setup and the direct current resistance monitored continuously.

Analysis of loss. The impedance of 1 m-long transmission lines was measured at a voltage amplitude of 1 V using an impedance analyzer (Zurich Instruments HF2LI Lock-in Amplifier). In this test, lines were interfaced to the instrument through a wire-to-BNC adapter on the near end, where the center and outer conductors were coupled to the positive and negative pole, respectively, and left in open circuit or short circuit configuration on the far end. The attenuation coefficient was calculated based on the short circuit impedance and the open circuit admittance, corresponding to the series resistive and inductive or shunt conductive and capacitive contributions, respectively, as described in ref. [51]. The measurements were carried out over the frequency range 10 kHz - 10 MHz, as higher frequencies could not be realized due to instrument limitations. While this frequency range does not encompass the entire bandwidth of the employed step in the time-domain, which for a 100 ps risetime extends into the GHz region, it allows to gain an insight into attenuation contributions and compare transmission line designs.

Time-domain reflectometry analysis. *General setup.* The near end of the transmission lines was connected to a wire-to-BNC adapter, and the far line end was terminated in an open circuit. The transmission lines were interrogated through a BNC interface by a digital sampling oscilloscope (Tektronix 11801C). Using the instrument, a voltage step of amplitude 0.5 V and with a rise time of approximately 100 ps was sent down the transmission lines and the resulting voltage transient across the lines recorded. The internal resistance of the instrument is 50 Ω.

Shield characterization. The performance of the shield in soft transmission lines was evaluated by recording the time-domain reflectometry waveforms of 1 m-long lines, which were successively submersed in ethanol and deionized water for line sections 40 cm – 60 cm.

Pressing response test. For characterizing the response to pressing force magnitude, the triangular liquid metal transmission lines of length 1 m were compressed locally at a position of 50 cm using the same setup and configuration as in the direct current measurements, and the waveforms recorded continuously. Due to larger necessary forces, the triangular solid metal lines were compressed using a motorized force tester (Mecmesin Multitest 2.5-I stand with Mecmesin Basic Force Gauge load cell) at a controlled displacement of 1 mm min^{-1}, where also a steel rod of diameter 6 mm served as an indenter. The force-dependent induced reflections in the waveforms were quantified by a series resistance and a shunt capacitance for the liquid metal and solid metal lines, respectively, as described in Supplementary Note 4. For characterizing the response to pressure position, 1 m-long triangular liquid metal transmission lines were manually compressed at predetermined positions using the steel rod at a force that induced a reflection of amplitude 0.1 V, and the respective waveforms recorded. For the test involving multiple pressure points, vises were used to compress a 1 m-long line at positions 33 cm and 66 cm at a force magnitude that induced 50 mV reflections in the waveform, which was used to calculate the distributed resistance (Supplementary Note 5). The spatial resolution of the pressure sensing was assessed by applying two pressure points resulting in 50 mV reflections with the vises on a 6 m-long triangular line. The position, corresponding to the distance from the interrogated line end to the first pressure point, and the spacing between the two pressure points were varied. The position-dependent spatial resolution was defined as the spacing for which the corresponding resistance distribution exhibited a valley between the two peaks equal to 70 % of the higher of the peaks.

Stretching response test. Triangular liquid metal transmission lines of length 1 m were elongated in a custom linear translation stage and the waveforms recorded for controlled displacements. For the localized strain test, the 1 m-long lines were locally compressed by custom clamps at positions 33 cm and 66 cm at a force magnitude that resulted in 50 mV reflections. The line sections were selectively stretched by hand and the waveforms recorded.

Electronic textile. *Assembly.* A 10 m-long triangular liquid metal transmission line was placed in a serpentine pattern with a spacing of 3 cm on a stretchable fabric of size 50 cm x 50 cm. The line loops were fixed in placed using Velcro strips that were glued on two sides of the fabric. The line was interfaced through a wire-to-BNC adapter on one end and left in open circuit configuration on the other end. A custom square wave generator in conjunction with a standard oscilloscope (Tektronix MDO3014) were used to interrogate the line. The recorded waveforms were transferred to a PC, where they were processed in real time by an algorithm (MathWorks MATLAB) to extract the variable line length and distributed resistance. Since the propagation speed is known for the dielectric SEBS, no calibration for the localization of stimuli is necessary.

Testing. For approximating the spatial resolution, the line was locally compressed in 25 cm steps for the entire length, and the overlap of distributed resistance peaks assessed. For the pressing test, pressures were applied with fingers at arbitrary positions along the line. For the stretching test, metal rods were fixed on two sides of the textile orthogonally to the line, and pulled apart and brought back together. The captured waveforms were continuously recorded and processed during all the tests.

Data availability

The datasets generated and analyzed in the current study are available from the corresponding author on reasonable request.

Code availability

The code for the real-time data processing of the electronic textile and other findings of this study are available from the corresponding authors upon reasonable request.

Acknowledgments

The authors thank Lukas Riemer, Zhaoyang Wang, Dr. Hamidreza Karami, and Prof. Farhad Rachidi-Haeri for experimental support. The authors acknowledge Kraton Polymers for providing the material SEBS. The authors also acknowledge the European Research Council (ERC Starting Grant 679211 "FLOWTONICS") for funding this project.

References

1. Niu, S. *et al.* A wireless body area sensor network based on stretchable passive tags. *Nat. Electron.* **2**, 361–368 (2019).
2. Liu, J. J. *et al.* BreathSens: A Continuous On-Bed Respiratory Monitoring System with Torso Localization Using an Unobtrusive Pressure Sensing Array. *IEEE J. Biomed. Heal. Informatics* **19**, 1682–1688 (2015).
3. Choi, S. *et al.* Highly conductive, stretchable and biocompatible Ag–Au core–sheath nanowire composite for wearable and implantable bioelectronics. *Nat. Nanotechnol.* **13**, 1048–1056 (2018).
4. Wang, X., Gu, Y., Xiong, Z., Cui, Z. & Zhang, T. Silk-Molded Flexible, Ultrasensitive, and Highly Stable Electronic Skin for Monitoring Human Physiological Signals. *Adv. Mater.* **26**, 1336–1342 (2014).
5. Gerratt, A. P., Michaud, H. O. & Lacour, S. P. Elastomeric Electronic Skin for Prosthetic Tactile Sensation. *Adv. Funct. Mater.* **25**, 2287–2295 (2015).
6. Lin, L. *et al.* Triboelectric Active Sensor Array for Self-Powered Static and Dynamic Pressure Detection and Tactile Imaging. *ACS Nano* **7**, 8266–8274 (2013).
7. Jung, S. *et al.* Wearable Fall Detector using Integrated Sensors and Energy Devices. *Sci. Rep.* **5**, 1–9 (2015).
8. Welch, Harnett & Lee. A Review on Measuring Affect with Practical Sensors to Monitor Driver Behavior. *Safety* **5**, 72 (2019).
9. Zhao, H., O'Brien, K., Li, S. & Shepherd, R. F. Optoelectronically innervated soft prosthetic hand via stretchable optical waveguides. *Sci. Robot.* **1**, eaai7529 (2016).
10. Markvicka, E. J., Bartlett, M. D., Huang, X. & Majidi, C. An autonomously electrically self-healing liquid metal–elastomer composite for robust soft-matter robotics and electronics. *Nat. Mater.* **17**, 618–624 (2018).
11. Boutry, C. M. *et al.* A hierarchically patterned, bioinspired e-skin able to detect the direction of applied pressure for robotics. *Sci. Robot.* **3**, eaau6914 (2018).
12. Lipomi, D. J. *et al.* Skin-like pressure and strain sensors based on transparent elastic films of carbon nanotubes. *Nat. Nanotechnol.* **6**, 788–792 (2011).
13. Park, J. *et al.* Giant Tunneling Piezoresistance of Composite Elastomers with Interlocked Microdome Arrays for Ultrasensitive and Multimodal Electronic Skins. *ACS Nano* **8**, 4689–4697 (2014).
14. Atalay, A. *et al.* Batch Fabrication of Customizable Silicone-Textile Composite Capacitive Strain Sensors for Human Motion Tracking. *Adv. Mater. Technol.* **2**, 1700136 (2017).
15. Liu, M. *et al.* Large-Area All-Textile Pressure Sensors for Monitoring Human Motion and Physiological Signals. *Adv. Mater.* **29**, 1703700 (2017).
16. Atalay, O., Kennon, W. R. & Demirok, E. Weft-Knitted Strain Sensor for Monitoring Respiratory Rate and Its Electro-Mechanical Modeling. *IEEE Sens. J.* **15**, 110–122 (2015).
17. Rothmaier, M., Luong, M. P. & Clemens, F. Textile Pressure Sensor Made of Flexible Plastic Optical Fibers. *Sensors* **8**, 4318–4329 (2008).
18. Nguyen-Dang, T. *et al.* Controlled Sub-Micrometer Hierarchical Textures Engineered in

Polymeric Fibers and Microchannels via Thermal Drawing. *Adv. Funct. Mater.* **27**, 1605935 (2017).
19. Leber, A. *et al.* Compressible and Electrically Conducting Fibers for Large-Area Sensing of Pressures. *Adv. Funct. Mater.* 1904274 (2019). doi:10.1002/adfm.201904274
20. Leber, A., Cholst, B., Sandt, J., Vogel, N. & Kolle, M. Stretchable Thermoplastic Elastomer Optical Fibers for Sensing of Extreme Deformations. *Adv. Funct. Mater.* **29**, 1802629 (2018).
21. Cooper, C. B. *et al.* Stretchable Capacitive Sensors of Torsion, Strain, and Touch Using Double Helix Liquid Metal Fibers. *Adv. Funct. Mater.* **27**, 1605630 (2017).
22. Yan, W. *et al.* Advanced Multimaterial Electronic and Optoelectronic Fibers and Textiles. *Adv. Mater.* **31**, 1802348 (2019).
23. Furse, C., Chung, Y. C., Lo, C. & Pendayala, P. A critical comparison of reflectometry methods for location of wiring faults. *Smart Struct. Syst.* **2**, 25–46 (2006).
24. Smail, M. K., Pichon, L., Olivas, M., Auzanneau, F. & Lambert, M. Detection of Defects in Wiring Networks Using Time Domain Reflectometry. *IEEE Trans. Magn.* **46**, 2998–3001 (2010).
25. Zhou, Z., Jiao, T., Zhao, P., Liu, J. & Xiao, H. Development of a Distributed Crack Sensor Using Coaxial Cable. *Sensors* **16**, 1198 (2016).
26. Lin, M. W., Thaduri, J. & Abatan, A. O. Development of an electrical time domain reflectometry (ETDR) distributed strain sensor. *Meas. Sci. Technol.* **16**, 1495–1505 (2005).
27. Dominauskas, A., Heider, D. & Gillespie, J. W. Electric time-domain reflectometry distributed flow sensor. *Compos. Part A Appl. Sci. Manuf.* **38**, 138–146 (2007).
28. Pandey, G., Deffor, H., Thostenson, E. T. & Heider, D. Smart tooling with integrated time domain reflectometry sensing line for non-invasive flow and cure monitoring during composites manufacturing. *Compos. Part A Appl. Sci. Manuf.* **47**, 102–108 (2013).
29. Roelvink, J., Trabelsi, S. & Nelson, S. O. A planar transmission-line sensor for measuring the microwave permittivity of liquid and semisolid biological materials. *IEEE Trans. Instrum. Meas.* **62**, 2974–2982 (2013).
30. Qu, Y. *et al.* Superelastic Multimaterial Electronic and Photonic Fibers and Devices via Thermal Drawing. *Adv. Mater.* **30**, 1707251 (2018).
31. Yeo, J. C. *et al.* Triple-State Liquid-Based Microfluidic Tactile Sensor with High Flexibility, Durability, and Sensitivity. *ACS Sensors* **1**, 543–551 (2016).
32. Park, Y.-L., Majidi, C., Kramer, R., Bérard, P. & Wood, R. J. Hyperelastic pressure sensing with a liquid-embedded elastomer. *J. Micromechanics Microengineering* **20**, 125029 (2010).
33. Anderson, A., Menguc, Y., Wood, R. J. & Newman, D. Development of the polipo pressure sensing system for dynamic space-suited motion. *IEEE Sens. J.* **15**, 6229–6237 (2015).
34. Hammond, F. L., Kramer, R. K., Wan, Q., Howe, R. D. & Wood, R. J. Soft tactile sensor arrays for force feedback in micromanipulation. *IEEE Sens. J.* **14**, 1443–1452 (2014).
35. Overvelde, J. T. B. *et al.* Mechanical and electrical numerical analysis of soft liquid-embedded deformation sensors analysis. *Extrem. Mech. Lett.* **1**, 42–46 (2014).
36. Park, Y. L., Chen, B. R. & Wood, R. J. Design and fabrication of soft artificial skin using embedded microchannels and liquid conductors. *IEEE Sens. J.* **12**, 2711–2718 (2012).
37. Mengüç, Y. *et al.* Wearable soft sensing suit for human gait measurement. *Int. J. Rob. Res.* **33**, 1748–1764 (2014).
38. Majidi, C., Kramer, R. & Wood, R. J. A non-differential elastomer curvature sensor for softer-than-skin electronics. *Smart Mater. Struct.* **20**, 105017 (2011).
39. Cataldo, A., De Benedetto, E. & Cannazza, G. *Broadband Reflectometry for Enhanced Diagnostics and Monitoring Applications*. **93**, (Springer Berlin Heidelberg, 2011).
40. Zandvakili, M., Honari, M. M., Mousavi, P. & Sameoto, D. Gecko-Gaskets for Multilayer, Complex, and Stretchable Liquid Metal Microwave Circuits and Antennas. *Adv. Mater. Technol.* **2**, 1700144 (2017).
41. Mohsen-Nia, M., Amiri, H. & Jazi, B. Dielectric Constants of Water, Methanol, Ethanol, Butanol and Acetone: Measurement and Computational Study. *J. Solution Chem.* **39**, 701–708 (2010).
42. Taylor, G. F. A Method of Drawing Metallic Filaments and a Discussion of their Properties and Uses. *Phys. Rev.* **23**, 655–660 (1924).

43. Rogers, J. A., Ghaffari, R. & Kim, D.-H. *Stretchable Bioelectronics for Medical Devices and Systems*. (Springer International Publishing, 2016). doi:10.1007/978-3-319-28694-5
44. Pozar, D. M. *Microwave Engineering*. (John Wiley & Sons, Inc., 2012).
45. Kaiser, K. L. *Transmission lines, matching, and crosstalk*. (Taylor & Francis, 2006).
46. Collier, R. J. *Transmission lines : equivalent circuits, electromagnetic theory, and photons*. (Cambridge University Press, 2013).
47. Sorin, F., Lestoquoy, G., Danto, S., Joannopoulos, J. D. & Fink, Y. Resolving optical illumination distributions along an axially symmetric photodetecting fiber. *Opt. Express* **18**, 24264–75 (2010).
48. Wadell, B. C. *Transmission line design handbook*. (Artech House, 1991).
49. Abouraddy, A. F. *et al.* Towards multimaterial multifunctional fibres that see, hear, sense and communicate. *Nat. Mater.* **6**, 336–347 (2007).
50. Xu, P. A. *et al.* Optical lace for synthetic afferent neural networks. *Sci. Robot.* **4**, eaaw6304 (2019).
51. Kharraz, M. A. O. *et al.* Experimental characterization of outdoor low voltage cables for narrowband power line communication. in *2016 International Symposium on Power Line Communications and its Applications (ISPLC)* 138–143 (IEEE, 2016). doi:10.1109/ISPLC.2016.7476267